

Thinking with Spatial Code for Physical-World Video Reasoning

Jieneng Chen^{1,*}, Wenxin Ma^{1,*}, Ruisheng Yuan^{1,*}, Yunzhi Zhang^{2,*}, Jiajun Wu^{2,†}, Alan Yuille^{1,†}

¹Johns Hopkins University ²Stanford University

Abstract

We introduce Thinking with Spatial Code, a framework that transforms RGB video into explicit, temporally coherent 3D representations for physical-world visual question answering. We highlight the empirical finding that our proposed spatial encoder can parse videos into structured spatial code with explicit 3D oriented bounding boxes and semantic labels, enabling large language models (LLMs) to reason directly over explicit spatial variables. Specifically, we propose the spatial encoder that encodes image and geometric features by unifying 6D object parsing and tracking backbones with geometric prediction, and we further finetuning LLMs with reinforcement learning using a spatial rubric reward that encourages perspective-aware, geometrically grounded inference. As a result, our model outperforms proprietary vision–language models on VSI-Bench, setting a new state-of-the-art. Code is available at <https://github.com/Beckschen/spatialcode>.

1. Introduction

Humans continuously perceive the physical world not as a sequence of disjointed frames, but as a coherent 3D environment that unfolds over time. From streams of visual inputs, we effortlessly parse spatial layouts, track objects, infer their dynamics, and reason about causal interactions. Achieving such spatially grounded understanding from video remains a long-standing challenge for machine intelligence. Despite the impressive progress of recent large multimodal models (MLMMs), their reasoning is primarily linguistic and appearance-based, lacking explicit 3D structure or spatial continuity. As a result, they can describe *what* they see but struggle to reason about *where* things are, *how* they are oriented relative to one another, and *when* they disappear and reappear – abilities essential for physical-world perception.

To bridge this gap, we introduce **Thinking-with-Spatial-Code**, a framework that transforms RGB video into explicit,

*Equal contribution †Equal advising ✉<jchen293@jh.edu>.

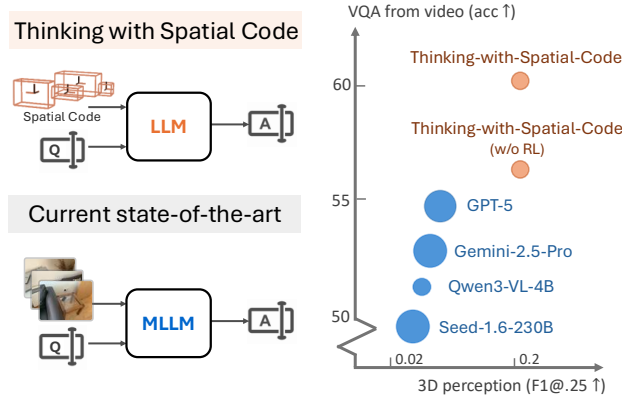


Figure 1. Thinking with Spatial Code enables superior spatial reasoning from video. *Left:* Unlike current state-of-the-art multimodal LLMs (MLLMs) that reason directly over the raw RGB image or video, our approach first parses video into explicit 3D spatial codes, then prompts a text-only LLM to reason over these symbolic descriptions. *Right:* On VSI-Bench (Yang et al., 2025b), our method fine-tuned on Qwen3-4B (Yang et al., 2025a) significantly outperforms leading MLLMs including GPT-5o, Gemini-2.5, and Qwen3-VL in video-spatial reasoning accuracy. Reinforcement learning with spatial rubric rewards further improves performance. Dot size indicates model scale (4B–230B parameters; GPT and Gemini sizes are undisclosed). This demonstrates that the quality of 3D spatial representation, rather than model scale alone, is the key bottleneck for spatial reasoning.

temporally coherent 3D representations for physical-world visual question answering. Our key insight is that the quality of spatial representation, rather than model scale alone, is the critical bottleneck for spatial reasoning. We highlight the empirical finding that the spatial encoders trained to parse videos into structured spatial codes — with explicit 3D bounding boxes and semantic labels — perform reliably on real-world distributions, enabling large language models to reason directly over explicit spatial variables.

Our framework consists of two main components. First, a **Spatial Encoder** transforms streaming video into structured spatial codes, each encoding an object’s semantic label, 3D position, size, and orientation. It integrates a dual-encoder architecture combining SAM-2 (Ravi et al., 2024) for object-level features and Depth Anything 3 (Lin et al., 2025) for geometric features, jointly performing segmentation, tracking, and 3D reconstruction. Second, we prompt LLMs with

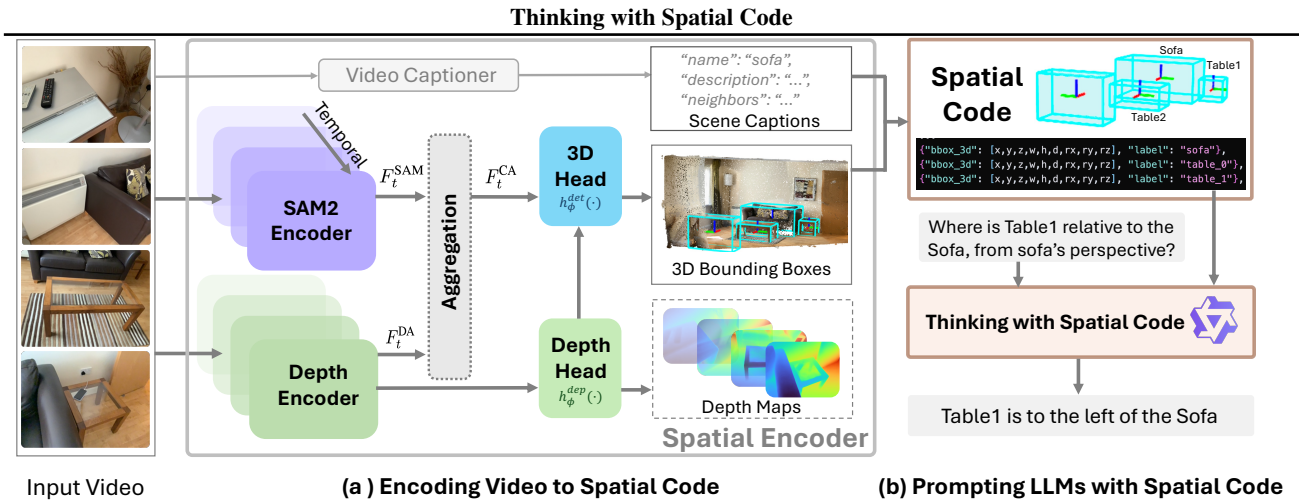


Figure 2. **Overview.** (a) **Encoding Video to Spatial Code:** The Spatial Encoder processes video through a dual-encoder architecture. The SAM-2 (Ravi et al., 2024) encoder extracts object-level features F_t^{SAM} with temporal attention, while the Depth Encoder (from Depth Anything 3 (Lin et al., 2025)) extracts spatial features F_t^{DA} . Cross-attention fuses these representations into F_t^{CA} , which feeds into a 3D Head for predicting 3D object bounding boxes with 3D orientation and a Depth Head for dense geometric supervision. Outputs are structured into symbolic spatial codes encoding object categories, positions, sizes, and orientations. (b) **Prompting LLMs with Spatial Code:** The spatial codes serve as explicit, interpretable inputs to LLMs for spatial reasoning. Given a query requiring perspective-aware understanding (e.g., “Where is Table1 relative to the Sofa, from sofa’s perspective?”), the LLM reasons directly over the structured 3D representations to produce geometrically grounded answers.

these symbolic spatial codes for spatial reasoning. This design enables LLMs to perform *thinking with spatial code* through explicit coordinate reasoning, while leveraging commonsense knowledge (e.g., understanding that “the front of a sofa” implies a canonical facing direction).

To further enhance reasoning capabilities, we employ reinforcement learning with a novel spatial rubric reward, motivated by careful empirical examination of pre-trained models’ behaviors. We observe that models often exhibit a reasoning-action disconnect: correctly analyzing spatial relationships in chain-of-thought but producing incorrect final answers. Our spatial rubric reward evaluates reasoning quality along multiple interpretable dimensions, including perspective-based reasoning, orientation awareness, and directional consistency, while penalizing common failure modes such as viewer-centric errors.

Comprehensive experiments demonstrate that Thinking-with-Spatial-Code achieves state-of-the-art results on VSI-Bench (Yang et al., 2025b), outperforming both proprietary MLLMs such as GPT-5o and Gemini-2.5, and open-source models including Qwen3-VL.

We summarize our contributions as follows:

- We introduce **Thinking-with-Spatial-Code**, a new paradigm that parses streaming video into explicit 3D spatial codes for LLM-based inference.
- We provide an empirical recipe for training a perception module that unifies dual visual encoding, 6D object parsing and tracking, and geometric densification to generate structured spatial codes from RGB video.

- We finetune LLMs for video VQA using spatial code with a novel **spatial rubric reward** that encourages perspective-aware, geometrically grounded reasoning.
- The model achieves state-of-the-art performance on VSI-Bench, and demonstrate the key finding that perception quality is a critical bottleneck for the spatial reasoning performance of MLLMs.

We will make our code, models and training recipe fully public to facilitate further research in this direction.

2. Thinking with Spatial Code

We study physical-world visual question answering (VQA) from videos. Given a spatial query \mathbf{x}^q in the form of text and a RGB video $\mathbf{x}^{\text{video}} \in \mathbb{R}^{3 \times H \times W \times T}$ of T frames and spatial resolution $H \times W$, the goal is to infer a text responses \mathbf{y} .

Canonical MLLMs approximate the conditional distribution $p(\mathbf{y} | \mathbf{x}^{\text{video}}, \mathbf{x}^q)$, heavily relying on final ground truth answers to learn during training. The sparse nature of such training signals makes the model susceptible to shortcut solutions that rely on 2D appearance cues or viewer-centric biases rather than recovering metric 3D structure.

We propose to explicitly introduce *spatial codes* \mathbf{c} , an explicit intermediate representation that captures 3D structures of scenes. Specifically,

$$p(\mathbf{y} | \mathbf{x}^{\text{video}}, \mathbf{x}^q) = \int p(\mathbf{y} | \mathbf{c}, \mathbf{x}^{\text{video}}, \mathbf{x}^q) p(\mathbf{c} | \mathbf{x}^{\text{video}}, \mathbf{x}^q) d\mathbf{c}. \quad (1)$$

The factorization allows for imposing dense supervision signals on \mathbf{c} (§2.1), is immediately compatible with the

interface of existing large language models (§2.2), and further benefits the isolation between perception errors and reasoning errors, which motivates reward designs for reinforcement-learning finetuning (§2.3).

In practice, rather than marginalizing over all possible spatial interpretations, we adopt a *perception-then-reasoning* paradigm that commits to a maximum a posteriori estimate, which reduces Equation (1) into the following:

$$\mathbf{c}^* = \arg \max_{\mathbf{c}} p(\mathbf{c} \mid \mathbf{x}^{\text{video}}, \mathbf{x}^q) \approx f_\phi(\mathbf{x}^{\text{video}}), \quad (2)$$

$$p(\mathbf{y} \mid \mathbf{x}^{\text{video}}, \mathbf{x}^q) \approx p_\theta(\mathbf{y} \mid \mathbf{c}^*, \mathbf{x}^q), \quad (3)$$

where f_ϕ is a Spatial Encoder that encodes pertinent information from input videos as explained in §2.1, and p_θ is the sampling distribution from an LLM that performs reasoning on discrete tokens of spatial code and natural language.

2.1. Encoding Videos into Spatial Code

We propose a **Spatial Encoder** module f_ϕ with neural parameters ϕ , that predicts spatial code from an input video $\mathbf{x}^{\text{video}}$ (Equation (2)), whose output $\mathbf{c} = f_\phi(\mathbf{x}^{\text{video}})$ has the form $\mathbf{c} = \{\mathbf{c}_i\}_{i=1}^n$, where each i typically corresponds to an object in a scene, with object count n varies across scenes. Each code $\mathbf{c}_i = (l_i, \mathbf{p}_i, \mathbf{s}_i, \mathbf{r}_i)$ consists of a semantic label string l_i , position $\mathbf{p}_i \in \mathbb{R}^3$, size $\mathbf{s}_i \in \mathbb{R}^3$, and orientation (quaternion) $\mathbf{r}_i \in \mathbb{R}^4$. A structured scene caption is inserted at the beginning of the code with global context and attributes information.

Scene Captioning. We first employ a MLLM as a video captioner to generate structured, scene-level captions. The extracted captions include (i) global scene context, (ii) object-level descriptions, and (iii) neighboring objects descriptions. These structured captions compose the initial part of spatial code, providing rich semantic information including object attributes and contextual interactions.

Feature Encoders. We adopt a dual-encoder design. For each input video frame with frame index t , we use the image encoder from SAM-2 (Ravi et al., 2024) to extract semantic feature F_{SAM}^t , and use the encoder from Depth Anything 3 (Lin et al., 2025) to produce 3D-aware feature F_{DA}^t . These features are fused via a sequence of cross-attention layers $f_{\text{CA}}(\cdot)$. Then a lightweight transformer-based tracker $f_{\text{track}}(\cdot)$ from SAM-2 (Ravi et al., 2024) processes the per-frame features across frames to maintain object identity:

$$F_{\text{CA}}^t = f_{\text{CA}}(F_{\text{SAM}}^t, F_{\text{DA}}^t), \quad F^t = f_{\text{track}}(F_{\text{CA}}^t, F^{t-1}). \quad (4)$$

3D Detection Head. As in SAM-2, we provide a 2D bounding box prompt \hat{b}_i with label l_i on the first frame of the video clips. With the temporal-spatial feature F^t from Equation (4), position \mathbf{p}_i^t , size \mathbf{s}_i^t , and orientation \mathbf{r}_i^t for the

t -th frame and the i -th object are predicted via a learnable 3D detection head $h_\phi^{\text{det}}(\cdot)$. As (Brazil et al., 2023), an additional 2D bounding box b_i^t is predicted at each time stamp to stabilize training. Additionally, objects may enter or exit the field of view in the video. We predict an appearance probability \tilde{p}_i^t for each object at frame t to indicate whether it is visible. Furthermore, this process is conditioned on depth feature $h_\phi^{\text{dep}}(F_{\text{DA}}^t)$ defined in Equation (6). Overall, the 3D detection head can be written as:

$$(\mathbf{p}_i^t, \mathbf{s}_i^t, \mathbf{r}_i^t, b_i^t, \tilde{p}_i^t) = h_\phi^{\text{det}}(F^t, h_\phi^{\text{dep}}(F_{\text{DA}}^t), \hat{b}_i). \quad (5)$$

Frame-wise predictions of the same object are merged at the scene-level based on 3D positions, forming the final spatial code \mathbf{c}_i for each object (see §C.1 for more details).

Depth Head. The supervision from 3D object detection for the 3D head is inherently sparse, providing regression targets only at the object level. Consequently, most regions in the scene, particularly background areas, contain limited geometric cues for learning robust features.

To address this, we adopt a depth head $h_\phi^{\text{dep}}(\cdot)$ that predicts dense and informative depth features. Subsequently, a lightweight decoder $h_\phi^{\text{dep-out}}$ transforms these enriched features into explicit depth maps:

$$D_t = h_\phi^{\text{dep-out}} \circ h_\phi^{\text{dep}}(F_{\text{DA}}^t). \quad (6)$$

At the same time, following (Wang et al., 2025a), camera parameters are also predicted by this head for supervision needs. The benefits of leveraging dense geometric supervision include (1) stabilizing learning in otherwise information-sparse regions, and (2) capturing fine-grained geometric relationships among objects at the pixel level. The benefits are empirically validated in §3.3.

Training Objective. Following (Brazil et al., 2023), the spatial encoder is trained end-to-end by a multi-task loss:

$$\begin{aligned} \mathcal{L}_{\text{spatial}} = & \underbrace{\mathcal{L}_{\text{2D-det}} + \mathcal{L}_{\text{pos}} + \mathcal{L}_{\text{size}} + \mathcal{L}_{\text{ori}} + \mathcal{L}_{\text{chamfer}}}_{\mathcal{L}_{\text{detection}}} \\ & + \underbrace{\mathcal{L}_{\text{camera}} + \mathcal{L}_{\text{depth}}}_{\mathcal{L}_{\text{geometry}}} + \mathcal{L}_{\text{tracking}}. \end{aligned} \quad (7)$$

The detection loss $\mathcal{L}_{\text{detection}}$ supervises frame-wise 3D bounding box predictions through multiple components: $\mathcal{L}_{\text{2D-det}}$ combines GIoU (Rezatofighi et al., 2019) and L1 losses for 2D box alignment; \mathcal{L}_{pos} enforces 3D position accuracy using L1 loss for projected 2D centers and Laplacian aleatoric uncertainty loss (Kendall & Gal, 2017) for depth; $\mathcal{L}_{\text{size}}$ applies L1 loss to predicted object dimensions; \mathcal{L}_{ori} supervises normalized quaternion representations with L1 loss; and $\mathcal{L}_{\text{chamfer}}$ ensures bidirectional corner-wise alignment between predicted and ground-truth 3D boxes.

The geometry loss $\mathcal{L}_{\text{geometry}}$ supervises dense spatial understanding: $\mathcal{L}_{\text{depth}}$ employs a scale-invariant loss with aleatoric uncertainty weighting and gradient regularization for pixel-wise depth prediction, while $\mathcal{L}_{\text{camera}}$ supervises camera parameter estimation through L1 losses.

Finally, $\mathcal{L}_{\text{tracking}}$ supervises the model’s object appearance prediction across frames, implemented as a binary classification loss to determine whether an object is present in a given frame. More details are presented in §C.4.

2.2. Prompting LLMs with Spatial Code

The spatial code \mathbf{c} predicted by the Spatial Encoder from §2.1 enables text-only LLMs to perform explicit coordinate-based reasoning on input videos. The inference procedure follows Equation (3) and is expanded below.

Let \mathbf{c}_i be the i -th object’s spatial code from the Spatial Encoder’s prediction \mathbf{c} . It is serialized into text:

$$\text{str}(\mathbf{c}_i) = \{ \text{"bbox_3d : } [\mathbf{p}_i, \mathbf{s}_i, \mathbf{r}_i], \text{label : } l_i \} \}, \quad (8)$$

and the LLM outputs response \mathbf{y} autoregressively via

$$p_{\theta}(\mathbf{y} \mid \mathbf{c}, \mathbf{x}^q) = \prod_{j=1}^L p_{\theta}(\mathbf{y}_j \mid \mathbf{y}_{<j, \text{str}(\mathbf{c}), \mathbf{x}^q}), \quad (9)$$

where L is the length of response with response tokens \mathbf{y}_j , and $\text{str}(\mathbf{c}) = \bigoplus_{i=1}^n \text{str}(\mathbf{c}_i)$ concatenates all spatial codes. The code \mathbf{c} is immediately interpretable by pre-trained LLM without finetuning, improving the LLM’s performance on spatial queries (e.g., “Can the lamp fit to the right of the table?”) through explicit coordinate reasoning.

2.3. Reinforcement Learning with Spatial Rubric Reward

To further improve the LLM reasoning policy, we employ RL finetuning. While standard RL with verifiable rewards (Lambert et al., 2024) relies solely on outcome-based verification, we augment it with domain-specific process supervision inspired by prior work on step-level rewards (Uesato et al., 2022; Lightman et al., 2023).

Our reward function combines the verifiable outcome (accuracy) reward with rule-based spatial rubrics that evaluate intermediate reasoning quality:

$$r(\mathbf{y} \mid \mathbf{x}) = \underbrace{r_{\text{acc}}(\mathbf{y}, a^*)}_{\text{accuracy}} + \underbrace{r_{\text{format}}(\mathbf{y})}_{\text{format compliance}} + \underbrace{r_{\text{rubric}}(\mathbf{y}, \mathbf{x})}_{\text{spatial rubrics}}, \quad (10)$$

where a^* is the ground-truth answer, \mathbf{y} is a model response, and \mathbf{x} is the input context. For the first term, $r_{\text{acc}} = 1$ if the answer extracted from response \mathbf{y} matches a^* , and 0 otherwise. The format compliance term r_{format} rewards responses following the expected structure (e.g., concluding

with “Final Answer: [A/B/C/D]”) and penalizes degenerate repetition patterns. The last term is explained below.

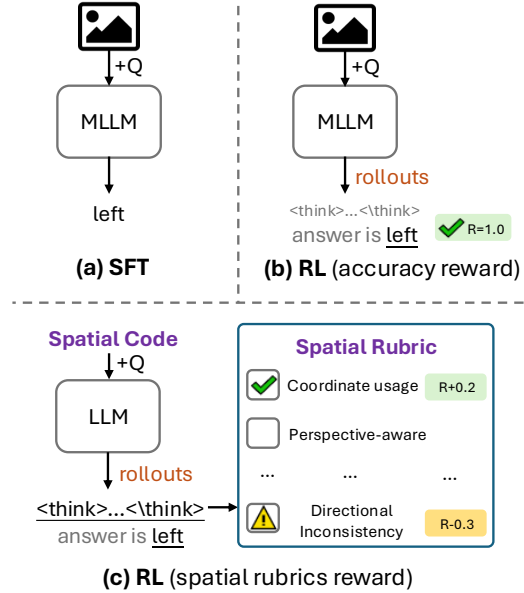


Figure 3. Comparison of Spatial Rubric Reward (c) against conventional SFT (a) and RL (b). Unlike traditional methods, our framework utilizes the 3D spatial codes as primary input. Applying a structured spatial rubric reward to model rollouts significantly improves the quality of spatial reasoning.

Spatial Rubric Reward. The spatial rubric term r_{rubric} in Equation (10) evaluates reasoning quality through a weighted sum of binary indicator functions:

$$r_{\text{rubric}}(\mathbf{y}, \mathbf{x}) = \sum_{i=1}^K w_i \cdot \psi_i(\mathbf{y}, \mathbf{x}), \quad (11)$$

where $\psi_i : (\mathbf{y}, \mathbf{x}) \rightarrow \{0, 1\}$ detects whether the response \mathbf{y} exhibits reasoning pattern i , and $w_i \in \mathbb{R}$ assigns positive weights to desired behaviors and negative weights to failure modes. The indicators $\{\psi_i\}$ are task-specific and target common spatial reasoning errors: (1) *world-coordinate confusion* — using global axes instead of object-centric coordinates; (2) *missing coordinate transformation* — skipping local reference frame construction; (3) *reasoning-answer inconsistency* — correct intermediate analysis but wrong final answer. For example, in the relative direction task, we reward explicit construction of local basis vectors ($w = +0.25$) and penalize direct mapping from world coordinates ($w = -0.25$). The total reward is clipped to $[-0.5, 1.8]$. Details are provided in §A.3.

Training Objective. We finetune pre-trained LLMs using GRPO (Shao et al., 2024), which computes advantages by comparing multiple sampled responses. For each prompt \mathbf{x} , we sample G responses $\{\mathbf{y}^{(i)}\}_{i=1}^G$ and compute group-

normalized advantages:

$$A^{(i)} = \frac{r(\mathbf{y}^{(i)}|\mathbf{x}) - \mu_G}{\sigma_G + \epsilon}, \quad (12)$$

where μ_G and σ_G are the mean and standard deviation of rewards within the group, and ϵ is a small constant for numerical stability. The policy π_θ is optimized via:

$$\mathcal{L}_{\text{GRPO}}(\theta) = \mathbb{E} \left[\sum_{i=1}^G A^{(i)} \log \pi_\theta(\mathbf{y}^{(i)}|\mathbf{x}) \right] - \beta \cdot D_{\text{KL}}[\pi_\theta \| \pi_{\text{ref}}], \quad (13)$$

where β controls the KL penalty against a reference policy π_{ref} , which is the frozen Qwen3-4B (Yang et al., 2025a).

3. Experiments

We evaluate the framework on video spatial reasoning (§3.1) and video 3D perception (§3.2) benchmarks, followed by ablation studies (§3.3) and analysis (§3.4).

3.1. Spatial Reasoning from Video Inputs

The task requires model to reason about object attributes, relations, and dynamics in space and time from video inputs.

Benchmarks. We evaluate on **VSI-Bench** (Yang et al., 2025b), which provides evaluation across: object counting, absolute/relative distance, object/room size, relative direction, route planning, and appearance order. The input for baseline models is RGB videos, and we require the model to output answers with reasoning. We further introduce **Video-RoboSpatial**, a benchmark for spatial reasoning over continuous video streams with annotated 6D object states, with particular emphasis on precise 3D orientation. Built upon ARKitScenes (Baruch et al., 2021), it extends RoboSpatial (Liang et al., 2024) question templates to video. For ambiguity avoidance, we by default give the model explicit 2D bounding boxes for identifying objects of interests.

Baselines. We compare against: (1) *proprietary MLLMs*: GPT-4o (Hurst et al., 2024), GPT-5o, Gemini-1.5/2.5-Pro (Comanici et al., 2025), Grok-4, and Seed-1.6; (2) *spatial-centric VLMs*: SpatialLadder (Li et al., 2025b), Spatial-MLLM (Wu et al., 2025), and SpaceR (Ouyang et al., 2025); (3) *open-source VLMs*: LLaVA-Video (Lin et al., 2024), LLaVA-OneVision (Li et al., 2025a), and Qwen-VL series (Bai et al., 2025; Yang et al., 2025a).

Results. As shown in Table 1, even without RL training, Thinking with Spatial Code improves over the Qwen3-VL-4B baseline by 1.6%. When additionally provided with 2D bounding box annotations, performance reaches **56.5%**, surpassing GPT-5o (55.0%), Gemini-2.5-Pro (53.5%), and Qwen3-VL-8B (55.0%). Compared to the non-RL counterparts, incorporating the spatial rubric reward yields consistent gains of **+3.4%** (without 2D boxes) and **+3.5%**

(with 2D boxes), demonstrating the effectiveness of RL training with perspective-aware spatial reasoning supervision. On Video-RoboSpatial, Thinking with Spatial Code achieves **67.0%** on configuration reasoning, outperforming the second-best method (GPT-5) by **6.7%**.

3.2. 3D Perception from Video Inputs

We evaluate the perception capability of the Spatial Encoder, comparing it with several recent SOTA perception models.

Setup. Evaluation is conducted on the test set of ARKitScenes (Baruch et al., 2021) (549 scenes) and the VSI-bench subset of ScanNet (Dai et al., 2017) (88 scenes) using scene-wise F1 scores at IoU thresholds of 0.25 (F1@.25) and 0.5 (F1@.5). For ARKitScenes, we use oriented bounding boxes for IoU calculation. For ScanNet, we use axis-aligned IoU due to inconsistent orientation annotations in the dataset. We compare against: (1) *image-based 3D detectors*: 3D-MOOD (Yang et al., 2025c) and DetAny3D (Zhang et al., 2025); (2) *point-cloud methods*: SpatialLM (Mao et al., 2025) and SceneScript (Avetisyan et al., 2024); (3) *MLLMs*: Qwen3-VL (Yang et al., 2025a). For methods with frame-wise predictions, we aggregate all predictions at the scene level by Non-Maximum Suppression. Bounding boxes are matched with the ground truth using the Hungarian algorithm for evaluation.

Results. As shown in Table 2, our Spatial Encoder achieves state-of-the-art results across both datasets. On ARKitScenes, we achieve F1@0.25 of 0.156 scene-wise, surpassing previous image-based methods by at least 0.06. On ScanNet scene-wise evaluation, we reach F1@0.25 of 0.209, significantly outperforming DetAny3D (0.119) and Qwen3-VL-235B (0.087). Notably, despite relying solely on video inputs, our method surpasses point-cloud-based approaches that operate on explicit 3D geometry on both datasets. These results demonstrate that our spatial encoder effectively maintains spatial-temporal consistency and produces more accurate 3D spatial codes.

3.3. Ablation Studies

Spatial Encoder Design. Table 3 ablates the encoder architecture. We evaluate localization accuracy by F1@.25, 3D IoU, metric depth error, and scale error. Using only SAM-2 yields poor F1@.25 at 0.27 and large depth error at 0.5. Incrementally adding depth loss and depth head improves performance, achieving the highest F1@.25 (+0.05) and lowest depth error (-0.19).

Spatial Rubric Reward. Table 4 compares training strategies. The spatial rubric reward achieves the largest gains on direction-sensitive tasks (+31.6% on Rel. Dir.), confirming it encourages perspective-aware reasoning.

Thinking with Spatial Code

Table 1. Video spatial reasoning results on VSI-Bench and Video-RoboSpatial. Thinking with Spatial Code achieves state-of-the-art performance, outperforming proprietary MLLMs (e.g., GPT-5o) and spatial-centric methods. Gray rows indicate fair comparisons.

Methods	Size	VSI-Bench (Yang et al., 2025b)									Video-RoboSpatial
		Avg.	Obj. Count	Abs. Dist.	Obj. Size	Room Size	Rel. Dist.	Rel. Dir.	Route Plan	Appear. Order	Config.
Human Level	–	79.2	84.3	47.0	60.4	45.9	94.7	95.8	95.8	100	92.1
<i>Proprietary MLLMs</i>											
Seed-1.6	230B	49.9	43.5	34.3	66.1	<u>52.8</u>	55.0	35.7	44.3	67.9	54.3
Gemini-1.5 Pro	–	48.8	49.6	30.9	64.1	49.4	51.3	48.1	42.0	68.0	–
Gemini-2.5-Pro	–	53.5	46.0	37.3	<u>68.7</u>	54.3	61.9	43.9	<u>47.4</u>	68.7	53.3
GPT-4o	–	34.0	46.2	5.3	43.8	38.2	37.0	41.3	31.5	28.5	53.0
GPT-5	–	55.0	53.3	34.4	73.3	47.5	<u>63.7</u>	48.6	50.2	68.9	60.3
<i>Spatial-centric MLLMs</i>											
SpatialLadder (Li et al., 2025b)	3B	44.8	62.1	35.3	61.9	41.4	45.6	46.4	27.3	38.5	49.3
Spatial-MLLM (Wu et al., 2025)	4B	46.3	<u>66.6</u>	38.0	63.6	35.4	40.4	48.2	32.9	44.3	49.0
SpaceR (Ouyang et al., 2025)	7B	41.5	44.5	24.7	53.5	37.3	41.9	46.1	29.3	54.8	56.0
<i>Open-source MLLMs</i>											
LLaVA-Video (Lin et al., 2024)	7B	35.6	48.5	14.0	47.8	24.2	43.5	42.4	34.0	30.6	52.0
LLaVA-Video (Lin et al., 2024)	72B	40.9	48.9	22.8	57.4	35.3	42.4	36.7	35.0	48.6	58.0
LLaVA-OneVision (Li et al., 2025a)	7B	32.4	47.7	20.2	47.4	12.3	42.5	35.2	29.4	24.4	54.3
LLaVA-OneVision (Li et al., 2025a)	72B	40.2	43.5	23.9	57.6	37.5	42.5	39.9	32.5	44.6	56.0
Qwen2.5-VL (Bai et al., 2025)	7B	32.3	32.8	18.1	43.8	31.7	38.0	37.4	28.3	27.9	49.7
Qwen3-VL (Yang et al., 2025a)	8B	55.0	52.1	44.7	60.4	43.1	56.6	56.3	38.1	70.2	48.0
Qwen3-VL (Yang et al., 2025a)	4B	52.8	53.1	46.3	63.4	48.0	53.3	49.9	37.1	58.9	52.7
Qwen3-VL (Yang et al., 2025a) + 2D box	4B	54.5	66.6	42.3	57.8	40.8	56.9	52.7	37.6	66.9	52.7
Thinking with Spatial Code (w/o RL)	4B	54.6	58.3	37.0	71.2	52.4	54.2	50.2	35.6	63.9	65.3
Thinking with Spatial Code (w/o RL) + 2D box	4B	56.5	95.2	<u>50.0</u>	50.9	19.9	63.7	55.5	25.3	58.4	<u>65.3</u>
Thinking with Spatial Code	4B	<u>57.0</u>	58.3	39.0	<u>73.0</u>	52.4	57.8	<u>55.9</u>	38.7	63.9	67.0
Thinking with Spatial Code + 2D box	4B	60.0	95.2	60.7	50.8	33.1	62.0	87.1	32.5	59.0	67.0

Table 2. Video 3D perception performance comparison. Our Spatial Encoder achieves state-of-the-art performance on scene-level F1, demonstrating strong spatial-temporal consistency. Image-based detectors operate on single frames and to support video input we aggregate predictions across frames. Point-cloud-based detectors such as SceneScript require ground-truth point clouds as input (video support is not yet open-sourced). MLLMs process videos as sequences of image frames. No existing open-source method supports video 3D perception; our approach fills this gap.

Input	Methods	ARKitScenes		ScanNet	
		F1@.25	F1@.5	F1@.25	F1@.5
Image detector	3D-MOOD (Yang et al., 2025c)	0.066	0.009	0.083	0.025
	DetAny3D (Zhang et al., 2025)	0.094	0.012	0.119	0.024
Point-cloud detector	SpatialLM (Mao et al., 2025)	<u>0.122</u>	<u>0.055</u>	<u>0.134</u>	0.025
	SceneScript (Avetisyan et al., 2024)	0.020	0.014	0.101	<u>0.043</u>
MLLMs	Qwen3-VL-4B (Yang et al., 2025a)	0.041	0.011	0.077	0.023
	Qwen3-VL-235B (Yang et al., 2025a)	0.034	0.008	0.087	0.028
Video detector	Spatial Encoder (Ours)	0.156	0.082	0.209	0.062

3.4. Key Finding: Perception Quality Bounds Reasoning

A central finding work is that **spatial reasoning performance is largely determined by 3D perception quality**, not LLM capacity alone. Evidence is provided below.

Table 3. Ablation on encoder design. Dep. Err.: Depth Error. Scale Err.: Scale Error.

SAM2 Enc.	DA3 Enc.	Depth Head	F1@.25	3D IoU↑	Dep. Err.↓	Scale Err.↓
✓	–	–	0.27	0.10	0.50	0.63
✓	✓	–	0.31	0.12	0.42	0.57
✓	✓	✓	0.32	0.14	0.31	0.55

Table 4. Ablation on RL reward. Spatial rubric rewards yield large gains on direction and distance tasks.

Training	Avg.	Rel. Dir.	Abs. Dist.	Config.
w/o spatial code	51.8	48.8	42.6	47.0
w/o RL	56.5	55.5	50.0	65.3
w/ Accuracy Reward	57.6	59.3	52.3	63.0
w/ Spatial Rubric	60.0	87.1	60.7	67.0

Ground-Truth (GT) vs. Predicted Spatial Codes. Table 5 shows that with GT spatial codes, the same 4B LLM achieves **72.3%** accuracy, narrowing the human-machine gap. With predicted codes from our Spatial Encoder (F1@0.25≈0.52), accuracy drops to 60.0%. This 12.3% gap reflects perception errors propagating into reasoning.

Model Scale vs. Representation Quality. Figure 1 visualizes that MLLMs processing raw video (GPT-5o, Gemini-2.5, Qwen3-VL, Seed-1.6) plateau at 50–55% regardless of scale (4B to 230B parameters). In contrast, our 4B model

Table 5. **GT vs. predicted spatial codes.** The same LLM achieves 73.2% reasoning accuracy on VSI-Bench with perfect perception.

Spatial Code Source	RL	Perception	Reasoning
Ground-truth codes		1.00	68.9
Spatial Encoder (ours)		0.52	56.5
Ground-truth codes	✓	1.00	73.2
Spatial Encoder (ours)	✓	0.52	60.0
Human performance		–	79.2

with explicit spatial codes achieves 60.0%—and 73.2% with GT codes. This 10%+ gap between spatial-code reasoning and the best MLLMs demonstrates that **representation quality, not parameter count, is the limiting factor.**

Implication. Recall the factorization in Equation (1). These findings confirm that errors in the perception model $p(c | x^{\text{video}})$ propagate directly to reasoning, indicating that 3D perception remains a bottleneck for spatial reasoning.

3.5. Implementation Details

Spatial Encoder. The training dataset includes: CA-1M (Lazarow et al., 2025) (439K objects, 200M frames), Hyperism (Roberts et al., 2021) (40K objects, 60K frames), and Aria Digital Twin (Pan et al., 2023) (24K objects, 254K frames). Both encoders are frozen, and the prediction heads are trained on $4 \times$ A100 GPUs with a batch size of 4 for 800k steps (about 10 days). We use AdamW optimizer and cosine scheduler with a initial learning rate of $1e-4$. The ablation study is conducted on a subset of CA-1M. More details are provided in §C.

Additionally, we provide a training-free implementation of the spatial encoder. Bounding boxes are acquired by lifting SAM2 predictions into 3D and clustering based on lifted points. The implementation details are provided in §C.5.

Reinforcement Learning. Qwen3-4B (Yang et al., 2025a) with GRPO, number of rollouts $G = 16$, $\beta = 0.01$, lr $1e-6$, $4 \times$ A100 GPUs, 1 day. Details are provided in §A.1.

3.6. Qualitative Analysis

Qualitative comparisons in Fig. 4 highlight three common failure modes of MLLMs that our method addresses: (1) perspective-aware reasoning (Fig. 4a), (2) orientation-aware reasoning (Fig. 4b), and (3) 3D distance estimation (Fig. 4c). These questions requires model to understand perspective change, object orientation, and metric distance, respectively. These are tasks that current MLLMs struggle with due to reliance on ambiguous 2D visual cues. In contrast, our spatial codes provide explicit 3D cues, which enables precise calculation and suppresses hallucination.

The examples illustrate why *explicit spatial representations* outperform end-to-end MLLMs: they eliminate visual am-

biguities and provide the LLM with precise geometric information for reasoning.

4. Related Work

Vision-Language Models. The development of VLMs has progressed from contrastive approaches like CLIP (Radford et al., 2021; Chen et al., 2024c) to MLLMs models (Alayrac et al., 2022; Li et al., 2023; Liu et al., 2024; Chen et al., 2024b; Li et al., 2025a). Recent efforts extend to video understanding through Video-LLaVA (Lin et al., 2024) and proprietary systems such as Gemini (Comanici et al., 2025) and Qwen-VL (Bai et al., 2025; Yang et al., 2025a). However, these models rely on 2D appearance features and lack explicit 3D geometric understanding, struggling with tasks requiring precise spatial localization or perspective-aware reasoning. Our work addresses this gap by augmenting VLMs with structured 3D spatial codes that provide geometric grounding.

Spatial Reasoning. To evaluate and improve spatial understanding, benchmarks have evolved from synthetic datasets like CLEVR (Johnson et al., 2017) and Spatial457 (Wang et al., 2025b) to realistic settings including SpatialBench (Cai et al., 2024), RoboSpatial (Liang et al., 2024), and video-based VSI-Bench (Yang et al., 2025b). Concurrent approaches such as SpaceR (Ouyang et al., 2025), SpatialLadder (Li et al., 2025b), and Spatial-MLLM (Wu et al., 2025) improve spatial reasoning through reinforcement learning or progressive training. SpatialVLM (Chen et al., 2024a) grounds VLMs with metric depth for spatial QA, but operates on single images without temporal consistency. These methods either lack explicit 3D grounding or do not handle video input. In contrast, our framework parses streaming video into temporally coherent 3D spatial codes, enabling reasoning over explicit geometric representations across frames.

Vision as Inverse Graphics. The paradigm of vision-as-inverse-graphics and analysis-by-synthesis (Yuille & Kersten, 2006) has inspired approaches from classical structure-from-motion (Schönberger & Frahm, 2016) to learning-based scene understanding (Wu et al., 2017a; Yao et al., 2018). MarrNet (Wu et al., 2017b) operationalizes this through a 2D–2.5D–3D pipeline. Recent advances include depth estimation models like Depth Anything (Yang et al., 2024; Lin et al., 2025), segmentation foundations such as SAM-2 (Ravi et al., 2024), and 3D detectors including 3D-MOOD (Yang et al., 2025c) and DetAny3D (Zhang et al., 2025). Building on these, structured scene representations like SceneScript (Avetisyan et al., 2024) and SpatialLM (Mao et al., 2025) generate symbolic 3D descriptions in natural language. However, these methods require point cloud input and are restricted to pre-defined object categories, with performance heavily dependent on

(a) Perspective-Aware Reasoning

Question:

If I am standing by the dishwasher and facing the table, is the washer to my front-left, front-right, back-left, or back-right?

Video Frames

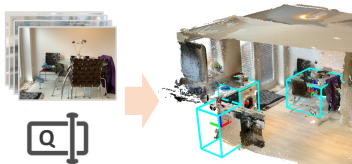


Gemini2.5 Pro

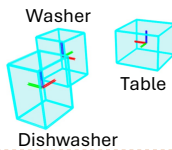
First, let's establish the layout of the kitchen based on the video. As seen from the entrance, the *left-hand* counter includes the ..., and **dishwasher** (00:25-00:29). The *back* counter includes ... the **washer** (00:43-00:47). The **dining table** is located in the area ..., past the washer (00:55-00:58). The observer is standing by the dishwasher. This places them *on the left side* of the kitchen. They are facing the table.... This means the observer's 'front' direction is across the kitchen *towards the back-right*. From the observer's position, the washer is both further into the room (in front) and to the right. Therefore, ..., the washer is *in the front-right quadrant*.

Final Answer: Front-Right ❌

Think with Spatial Code



Spatial Code



```
{
  "label": "washer",
  "bbox_3d": [-4.93, 0.22, -0.71, 0.44, 0.68, 0.89, 0, 0, -1.55]
},
{
  "label": "dishwasher",
  "bbox_3d": [-4.50, -0.95, -0.61, 0.52, 0.78, 0.91, 0, 0, -1.66]
},
{
  "label": "table",
  "bbox_3d": [-3.37, 1.63, -0.65, 0.75, 0.99, 0.68, 0, 0, -1.60]
}
```

Step1: identify objects

- Dishwasher: [-4.5006, -0.9568, -0.6117]
- Table: at [-3.3726, 1.6367, -0.6554]
- Washer: at [-4.9338, 0.2221, -0.7150]

Step2: Compute direction vector from dishwasher to table

$\Delta x = -3.373 - (-4.501) = 1.128$; $\Delta y = 1.637 - (-0.957) = 2.594$
 Forward vector: (1.128, 2.594)
 Magnitude = $\sqrt{1.128^2 + 2.594^2} \approx 2.828$
 Unit forward vector: (0.399, 0.917)
 Left vector (90° CCW rotation): (-0.917, 0.399)
 Right vector (90° CW rotation): (0.917, -0.399)

Step3: Calculate vector from dishwasher to washer

$\Delta x = -4.934 - (-4.501) = -0.433$; $\Delta y = 0.222 - (-0.957) = 1.179$
 Target vector: (-0.433, 1.179)

Step4: Determine direction

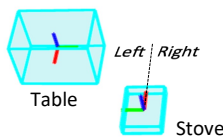
- Dot product with left vector: $(-0.433)(-0.917) + (1.179)(0.399) \approx 0.868$ ✓ Positive → LEFT
 - Dot product with forward vector: $(-0.433)(0.399) + (1.179)(0.917) \approx 0.908$ ✓ Positive → FRONT

Final Answer: Front-Left ✓

(b) Orientation-Aware Reasoning

Question

Is the table to the left or the right of the stove in the stove's local frame?

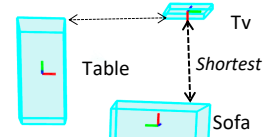


Gemini2.5 Pro: right ❌ Think with Spatial Code: Left ✓

(c) 3D Distance Estimation

Question

"Measuring from the closest point of each object, which of these objects (table, sofa) is the closest to the tv?"



Gemini2.5 Pro: table ❌ Think with Spatial Code: Sofa ✓

Figure 4. Qualitative comparison. We show three examples where Thinking with Spatial Code succeeds while Gemini 2.5 Pro fails. (a) **Perspective-aware reasoning with detailed reasoning trace:** The question requires model to reason from a specific observer viewpoint. Video-based models confuse absolute positions with observer-relative directions, while our spatial codes enable step-by-step coordinate transformation with precise calculation and significantly improves reasoning accuracy. (b) **Orientation-aware reasoning:** The question requires understanding object orientation (yaw angles). MLLMs rely on visual appearance, while our spatial codes provide explicit orientation parameters for accurate inference. (c) **3D distance estimation:** The task requires metric depth measurements. MLLMs use ambiguous 2D visual cues, while our spatial codes provide precise 3D coordinates for reliable distance calculation.

sensor quality. Our approach differs fundamentally: we operate directly on RGB video with open-vocabulary detection through natural language prompts, eliminating the dependency on 3D sensors while maintaining robust spatial

understanding through code-like geometric representations.

5. Conclusion

We introduced Thinking with Spatial Code, a framework that transforms RGB video into explicit 3D spatial representations for visual question answering from videos. We propose a Spatial Encoder architecture that unifies semantic and geometric understanding through a dual-encoder architecture, generating structured spatial codes that bridge perception and language reasoning. Combined with reinforcement learning using spatial rubric rewards on top of pre-trained LLMs, our approach achieves state-of-the-art performance on VSI-Bench, outperforming both proprietary and open-source VLMs. We will release our code, models, and training recipes to facilitate future research.

Acknowledgement

We gratefully acknowledge helpful discussions with Joshua Tenenbaum, Tianjian Li, Hao Chen, Sophia Qian, Daniel Khashabi, and Yana Wei in the early stages of this work.

References

- Alayrac, J.-B., Donahue, J., Luc, P., Miech, A., Barr, I., Hasson, Y., Lenc, K., Mensch, A., Millican, K., Reynolds, M., et al. Flamingo: a visual language model for few-shot learning. In *NeurIPS*, 2022.
- Avetisyan, A., Xie, C., Howard-Jenkins, H., Yang, T.-Y., Aroudj, S., Patra, S., Zhang, F., Frost, D., Holland, L., Orme, C., et al. Scenescrypt: Reconstructing scenes with an autoregressive structured language model. In *ECCV*, 2024.
- Bai, S., Chen, K., Liu, X., Wang, P., Yang, A., et al. Qwen2.5-vl technical report. *arXiv*, 2025.
- Baruch, G., Chen, Z., Dehghan, A., Dimry, T., Feigin, Y., Fu, P., Gebauer, T., Joffe, B., Kurz, D., Schwartz, A., et al. Arkitscenes: A diverse real-world dataset for 3d indoor scene understanding using mobile rgb-d data. *arXiv*, 2021.
- Brazil, G., Kumar, A., Straub, J., Ravi, N., Johnson, J., and Gkioxari, G. Omni3d: A large benchmark and model for 3d object detection in the wild. In *CVPR*, 2023.
- Cai, W., Liu, J., Zhang, Y., Wang, G., and Nie, W. Spatial-bench: Spatial understanding benchmark for 2d and 3d vision-language models. *arXiv*, 2024.
- Chen, B., Xu, Z., Kirmani, S., Ichter, B., Sadigh, D., Guibas, L., and Xia, F. Spatialvlm: Endowing vision-language models with spatial reasoning capabilities. In *CVPR*, 2024a.
- Chen, J., Ye, L., He, J., Wang, Z.-Y., Khashabi, D., and Yuille, A. Efficient large multi-modal models via visual context compression. *NeurIPS*, 2024b.
- Chen, J., Yu, Q., Shen, X., Yuille, A., and Chen, L.-C. Vitamin: Designing scalable vision models in the vision-language era. In *CVPR*, 2024c.
- Comanici, G., Bieber, E., Schaekermann, M., Pasupat, I., Sachdeva, N., Dhillon, I., Blistein, M., Ram, O., Zhang, D., Rosen, E., et al. Gemini 2.5: Pushing the frontier with advanced reasoning, multimodality, long context, and next generation agentic capabilities. *arXiv*, 2025.
- Dai, A., Chang, A. X., Savva, M., Halber, M., Funkhouser, T., and Nießner, M. Scannet: Richly-annotated 3d reconstructions of indoor scenes. In *CVPR*, 2017.
- Hurst, A., Lerer, A., Goucher, A. P., Perelman, A., Ramesh, A., Clark, A., Ostrow, A., Welihinda, A., Hayes, A., Radford, A., et al. Gpt-4o system card. *arXiv preprint arXiv:2410.21276*, 2024.
- Johnson, J., Hariharan, B., Van Der Maaten, L., Fei-Fei, L., Lawrence Zitnick, C., and Girshick, R. Clevr: A diagnostic dataset for compositional language and elementary visual reasoning. In *CVPR*, 2017.
- Kendall, A. and Gal, Y. What uncertainties do we need in bayesian deep learning for computer vision? *NeurIPS*, 2017.
- Kirillov, A., Mintun, E., Ravi, N., Mao, H., Rolland, C., Gustafson, L., Xiao, T., Whitehead, S., Berg, A. C., Lo, W.-Y., et al. Segment anything. In *ICCV*, 2023.
- Lambert, N., Morrison, J., Pyatkin, V., Huang, S., Ivison, H., Brahman, F., Miranda, L. J. V., Liu, A., Dziri, N., Lyu, S., et al. Tulu 3: Pushing frontiers in open language model post-training. *arXiv*, 2024.
- Lazarow, J., Griffiths, D., Kohavi, G., Crespo, F., and Dehghan, A. Cubify anything: Scaling indoor 3d object detection. In *CVPR*, 2025.
- Li, B., Zhang, Y., Guo, D., Zhang, R., Li, F., Zhang, H., Zhang, K., Zhang, P., Li, Y., Liu, Z., et al. Llava-onevision: Easy visual task transfer. *TMLR*, 2025a.
- Li, H., Li, D., Wang, Z., Yan, Y., Wu, H., Zhang, W., Shen, Y., Lu, W., Xiao, J., and Zhuang, Y. Spatialladder: Progressive training for spatial reasoning in vision-language models. *arXiv*, 2025b.
- Li, J., Li, D., Savarese, S., and Hoi, S. Blip-2: Bootstrapping language-image pre-training with frozen image encoders and large language models. In *ICML*, 2023.

- Liang, C. H., Hu, R.-Z., Wang, S., Yu, F., and Huang, D.-A. Robospacial: Teaching spatial understanding to 2d and 3d vision-language models for robotics. *arXiv*, 2024.
- Lightman, H., Kosaraju, V., Burda, Y., Edwards, H., Baker, B., Lee, T., Leike, J., Schulman, J., Sutskever, I., and Cobbe, K. Let’s verify step by step. In *ICLR*, 2023.
- Lin, B., Ye, Y., Zhu, B., Cui, J., Ning, M., Jin, P., and Yuan, L. Video-llava: Learning united visual representation by alignment before projection. In *EMNLP*, 2024.
- Lin, H., Chen, S., Liew, J., Chen, D. Y., Li, Z., Shi, G., Feng, J., and Kang, B. Depth anything 3: Recovering the visual space from any views. *arXiv*, 2025.
- Liu, H., Li, C., Wu, Q., and Lee, Y. J. Visual instruction tuning. In *NeurIPS*, 2024.
- Mao, Y., Zhong, J., Fang, C., Zheng, J., Tang, R., Zhu, H., Tan, P., and Zhou, Z. Spatiallm: Training large language models for structured indoor modeling. In *NeurIPS*, 2025.
- Ouyang, K., Liu, Y., Wu, H., Liu, Y., Zhou, H., Zhou, J., Meng, F., and Sun, X. Spacer: Reinforcing mllms in video spatial reasoning. *arXiv*, 2025.
- Pan, X., Charron, N., Yang, Y., Peters, S., Whelan, T., Kong, C., Parkhi, O., Newcombe, R., and Ren, Y. C. Aria digital twin: A new benchmark dataset for egocentric 3d machine perception. In *ICCV*, 2023.
- Radford, A., Kim, J. W., Hallacy, C., Ramesh, A., Goh, G., Agarwal, S., Sastry, G., Askell, A., Mishkin, P., Clark, J., et al. Learning transferable visual models from natural language supervision. In *ICML*, 2021.
- Ravi, N., Gabeur, V., Hu, Y.-T., Hu, R., Ryali, C., Ma, T., Khedr, H., Rädle, R., Rolland, C., Gustafson, L., et al. Sam 2: Segment anything in images and videos. *arXiv*, 2024.
- Rezatofghi, H., Tsoi, N., Gwak, J., Sadeghian, A., Reid, I., and Savarese, S. Generalized intersection over union: A metric and a loss for bounding box regression. In *CVPR*, 2019.
- Roberts, M., Ramapuram, J., Ranjan, A., Kumar, A., Bautista, M. A., Paczan, N., Webb, R., and Susskind, J. M. Hypersim: A photorealistic synthetic dataset for holistic indoor scene understanding. In *ICCV*, 2021.
- Schönberger, J. L. and Frahm, J.-M. Structure-from-motion revisited. In *CVPR*, 2016.
- Shao, Z., Wang, P., Zhu, Q., Xu, R., Song, J., Bi, X., Zhang, H., Zhang, M., Li, Y., Wu, Y., et al. Deepseekmath: Pushing the limits of mathematical reasoning in open language models. *arXiv*, 2024.
- Uesato, J., Kushman, N., Kumar, R., Song, F., Siegel, N., Wang, L., Creswell, A., Irving, G., and Higgins, I. Solving math word problems with process-and outcome-based feedback. *arXiv*, 2022.
- Wang, J., Chen, M., Karaev, N., Vedaldi, A., Rupprecht, C., and Novotny, D. Vggt: Visual geometry grounded transformer. In *CVPR*, 2025a.
- Wang, S., Leroy, V., Cabon, Y., Chidlovskii, B., and Revaud, J. Dust3r: Geometric 3d vision made easy. In *CVPR*, 2024.
- Wang, X., Ma, W., Zhang, T., de Melo, C. M., Chen, J., and Yuille, A. Spatial457: A diagnostic benchmark for 6d spatial reasoning of large multimodal models. In *CVPR*, 2025b.
- Wu, D., Fang, X., Liu, R., and Zhang, R. Spatial-mlm: Boosting mllm capabilities in visual-based spatial intelligence. *arXiv*, 2025.
- Wu, J., Tenenbaum, J. B., and Kohli, P. Neural scene de-rendering. In *CVPR*, 2017a.
- Wu, J., Wang, Y., Xue, T., Sun, X., Freeman, W. T., and Tenenbaum, J. B. MarrNet: 3D Shape Reconstruction via 2.5D Sketches. In *NeurIPS*, 2017b.
- Yang, A., Li, A., Yang, B., Zhang, B., Hui, B., Zheng, B., Yu, B., Gao, C., Huang, C., Lv, C., et al. Qwen3 technical report. *arXiv*, 2025a.
- Yang, J., Yang, S., Gupta, A. W., Han, R., Fei-Fei, L., and Xie, S. Thinking in space: How multimodal large language models see, remember, and recall spaces. In *CVPR*, 2025b.
- Yang, L., Kang, B., Huang, Z., Xu, X., Feng, J., and Zhao, H. Depth anything: Unleashing the power of large-scale unlabeled data. In *CVPR*, 2024.
- Yang, Y.-H., Piccinelli, L., Segu, M., Li, S., Huang, R., Fu, Y., Pollefeys, M., Blum, H., and Bauer, Z. 3d-mood: Lifting 2d to 3d for monocular open-set object detection. In *ICCV*, 2025c.
- Yao, S., Hsu, T. M., Zhu, J.-Y., Wu, J., Torralba, A., Freeman, B., and Tenenbaum, J. 3d-aware scene manipulation via inverse graphics. In *NeurIPS*, 2018.
- Yuille, A. and Kersten, D. Vision as Bayesian inference: analysis by synthesis? *Trends in Cognitive Sciences*, 2006.
- Zhang, H., Jiang, H., Yao, Q., Sun, Y., Zhang, R., Zhao, H., Li, H., Zhu, H., and Yang, Z. Detect anything 3d in the wild. In *ICCV*, 2025.

Supplementary Material

A. Reinforcement Learning Implementation Details

A.1. Training Hyperparameters

Table 6 summarizes the GRPO training hyperparameters used in our experiments.

Table 6. GRPO training hyperparameters.

Hyperparameter	Symbol	Value
<i>GRPO Algorithm</i>		
Group size (samples per prompt)	G	16
KL penalty coefficient	β	0.01
Sampling temperature	τ	0.7
Reward clipping range	–	$[-0.5, 1.8]$
<i>Optimization</i>		
Base model	–	Qwen3-4B-Instruct
Learning rate	η	1×10^{-6}
Batch size per device	–	4
Gradient accumulation steps	–	2
Number of GPUs	–	4
Effective batch size	B	32
Training epochs	–	1
<i>Sequence Length</i>		
Max prompt length	L_{prompt}	4096
Max completion length	L_{comp}	2048
<i>Infrastructure</i>		
Precision	–	BF16
Distributed strategy	–	DeepSpeed ZeRO-2
Gradient checkpointing	–	Enabled

A.2. Prompt Template

Our prompt template consists of four components: (1) system instructions with coordinate conventions, (2) 3D bounding box data, (3) task-specific instructions, and (4) the question with answer format. Figure 5 illustrates the overall structure.

Bounding Box Format. Each object is represented as a JSON dictionary with label and 3D bounding box parameters:

```
{"label": "cabinet", "bbox_3d":
[x_center, y_center, z_center,
x_size, y_size, z_size, roll, pitch, yaw]}
```

where $(x_{\text{center}}, y_{\text{center}}, z_{\text{center}})$ is the center position, $(x_{\text{size}}, y_{\text{size}}, z_{\text{size}})$ are di-

Prompt Structure Overview

1. System Instructions

“You are a multimodal reasoning model that interprets structured scene inputs...”

2. Coordinate System Conventions

“World Frame: Z-axis points Up. X and Y are horizontal.”

“Yaw: 0 rad is along +X. Positive Yaw is counter-clockwise.”

3. Measurement Definitions

“Object Size: $\max(x_{\text{size}}, y_{\text{size}}, z_{\text{size}})$ ”

“Distance: minimum Euclidean distance between closest points”

4. 3D Bounding Box Data (JSON format)

5. Task-Specific Instructions (varies by task type)

6. Question + Answer Format

Figure 5. High-level prompt structure for spatial reasoning tasks.

mensions, and `yaw` is the rotation around the Z-axis in radians.

Task-Specific Instructions. Table 7 summarizes the task-specific instructions injected into the prompt for each task type.

Table 7. Task-specific prompt instructions and answer formats.

Task Type	Key Instruction	Answer
<code>pairwise_configuration</code>	Focus on relative positions, orientations, left/right, front/behind	Yes/No
<code>object_rel_direction</code>	Analyze relative positions from object-centric perspective	A/B/C/D
<code>object_rel_distance</code>	Compare closest-point distances to multiple candidates	A/B/C/D
<code>object_abs_distance</code>	Calculate min distance between closest bbox points	Numeric
<code>object_counting</code>	Count objects matching specified category	Numeric
<code>object_size_estimation</code>	Report $\max(x_{\text{size}}, y_{\text{size}}, z_{\text{size}})$ in requested unit	Numeric
<code>room_size_estimation</code>	Estimate floor area from wall bounding boxes	Numeric
<code>obj_appearance_order</code>	Determine temporal order of first appearance in video	A/B/C/D
<code>route_planning</code>	Plan navigation with turn directions at waypoints	A/B/C/D

Example Prompt. Figure 6 shows a complete prompt for the `object_rel_direction` task.

A.3. Reward Function Details

Our reward function (Eq. 10) consists of three components: accuracy, format compliance, and spatial rubrics. Table 8 provides an overview of each component and its range.

You are a multimodal reasoning model that interprets structured scene inputs. You will be provided with a list of bounding boxes representing objects in the scene...

Coordinate System Conventions:

1. World Frame: Z-axis points Up. X and Y are horizontal.
2. Yaw: 0 rad is along +X. Positive Yaw is counter-clockwise.

Measurement Definitions:

1. Object Size: $\max(x_size, y_size, z_size)$
2. Absolute Distance: minimum Euclidean distance between closest points

IMPORTANT - Reading bbox_3d values:

The bbox_3d array format is: [x_center, y_center, z_center, x_size, y_size, z_size, roll, pitch, yaw]
- The YAW is the 9th (last) value - check it carefully!

The bounding boxes are:

```
{ "label": "bathtub",
  "bbox_3d": [-1.284, 1.547, 0.267, 0.812, 1.701, 0.534, 0, 0, 0] }
{ "label": "cabinet",
  "bbox_3d": [-0.065, 2.001, 1.003, 0.599, 0.593, 1.857, 0, 0, 0] }
{ "label": "washer",
  "bbox_3d": [0.632, 2.103, 0.429, 0.609, 0.571, 0.858, 0, 0, 0] }
```

Task Type: Object Relative Direction

You are analyzing the Object Relative Direction between two objects. Focus on their relative positions, orientations...

Based on the provided bounding boxes, answer the following question:

Standing at the bathtub, facing the cabinet, is the washer to your front-left, front-right, back-left, or back-right?

Options: A. front-right, B. back-right, C. front-left, D. back-left

Think step by step. Keep your reasoning concise (under 1000 words).

IMPORTANT: End your response with exactly:

Final Answer: A or Final Answer: B or Final Answer: C or Final Answer: D

Figure 6. Complete prompt example for the object_rel_direction task.

Format Compliance (r_{format}). Table 9 details the format compliance indicators that reward proper response structure and penalize degenerate outputs.

Base Reasoning Rubrics. Table 10 lists reasoning quality indicators applied across all spatial reasoning tasks.

Task-Specific Rubrics. We define specialized indicators for each task type. Tables 11 and 12 show rubrics for two representative tasks: object_rel_direction and pairwise_configuration.

A.4. Rubric Scoring Example

Figure 7 illustrates how the rubric reward distinguishes between correct answers achieved through proper spatial reasoning versus coincidental correctness. Both responses arrive at the same correct answer, but receive significantly

Table 8. Reward function components and their ranges.

Component	Range	Description
r_{acc}	$\{0, 1\}$	Exact match with ground truth a^*
r_{format}	$[-0.7, +0.1]$	Structure compliance and penalties
r_{rubric}	$[-0.65, +0.8]$	Task-specific reasoning quality
r_{total}	$[-0.5, 1.8]$	Clipped sum of all components

Table 9. Format compliance indicators.

Indicator	Condition	Weight
Valid format	Single "Final Answer:" with valid response	+0.1
Missing format	No "Final Answer:" detected	-0.2
Degenerate repetition	Pathological output patterns (e.g., repeated phrases)	-0.5
Excessive length	Response > 4000 characters	≤ -0.3
Too short	Response < 200 characters	-0.2

different rewards based on their reasoning methodology.

The "lucky guess" penalty ($w = -0.30$) is applied when the model arrives at the correct answer but fails to demonstrate proper spatial reasoning methodology—specifically, when $r_{\text{acc}} = 1$ but neither the local coordinate system indicator nor the vector projection indicator is satisfied. This design choice encourages learning of transferable reasoning skills that generalize across different spatial configurations.

✓ Proper Reasoning	✗ Flawed Reasoning	Reward Breakdown																																		
<p>Step 1: Extract coordinates. Bathub: $(-1.28, 1.55)$ Cabinet: $(-0.07, 2.00)$ Washer: $(0.63, 2.10)$</p> <p>Step 2: Compute facing direction. $\vec{v} = (-0.07, 2.00) - (-1.28, 1.55)$ $= (1.21, 0.45)$ Normalize: $\hat{f} = (0.94, 0.35)$</p> <p>Step 3: Build local coordinates. $\text{forward} = \hat{f} = (0.94, 0.35)$ $\text{right} = (\hat{f}_y, -\hat{f}_x) = (0.35, -0.94)$</p> <p>Step 4: Project washer position. $\vec{w} = (0.63, 2.10) - (-1.28, 1.55)$ $= (1.91, 0.55)$ $\text{front} = \vec{w} \cdot \hat{f} = 1.99 > 0$ ✓ $\text{right} = \vec{w} \cdot \hat{r} = 0.15 > 0$ ✓ Therefore, washer is front-right. Final Answer: A</p>	<p>Looking at the coordinates: Washer is at $(0.63, 2.10)$</p> <p>In world coordinates: $x = 0.63 > 0 \Rightarrow \text{right}$ $y = 2.10 > 0 \Rightarrow \text{front}$ So washer is front-right. Final Answer: A</p> <p style="color: red;">Error: Uses world coordinate axes directly ($+x \rightarrow \text{right}$) without constructing local reference frame from observer's position and facing direction.</p> <p style="color: red;">This approach fails when the observer faces a different direction.</p>	<table border="1"> <thead> <tr> <th>Component</th> <th>P</th> <th>F</th> </tr> </thead> <tbody> <tr> <td>r_{acc} (correct)</td> <td>+1.0</td> <td>+1.0</td> </tr> <tr> <td>r_{fmt} (format)</td> <td>+0.1</td> <td>+0.1</td> </tr> <tr> <td>Structured reason.</td> <td>+0.1</td> <td>0</td> </tr> <tr> <td>Coord. extraction</td> <td>+0.1</td> <td>+0.05</td> </tr> <tr> <td>Facing vector</td> <td>+0.15</td> <td>0</td> </tr> <tr> <td>Local coord. sys.</td> <td>+0.25</td> <td>0</td> </tr> <tr> <td>Vector projection</td> <td>+0.2</td> <td>0</td> </tr> <tr> <td>World-coord. conf.</td> <td>0</td> <td>-0.25</td> </tr> <tr> <td>Lucky guess pen.</td> <td>0</td> <td>-0.3</td> </tr> <tr> <td>Total</td> <td>+1.8</td> <td>+0.6</td> </tr> </tbody> </table>	Component	P	F	r_{acc} (correct)	+1.0	+1.0	r_{fmt} (format)	+0.1	+0.1	Structured reason.	+0.1	0	Coord. extraction	+0.1	+0.05	Facing vector	+0.15	0	Local coord. sys.	+0.25	0	Vector projection	+0.2	0	World-coord. conf.	0	-0.25	Lucky guess pen.	0	-0.3	Total	+1.8	+0.6	
Component	P	F																																		
r_{acc} (correct)	+1.0	+1.0																																		
r_{fmt} (format)	+0.1	+0.1																																		
Structured reason.	+0.1	0																																		
Coord. extraction	+0.1	+0.05																																		
Facing vector	+0.15	0																																		
Local coord. sys.	+0.25	0																																		
Vector projection	+0.2	0																																		
World-coord. conf.	0	-0.25																																		
Lucky guess pen.	0	-0.3																																		
Total	+1.8	+0.6																																		

Figure 7. Rubric scoring comparison for `object_rel_direction`. Both responses achieve the correct answer (A: front-right), but the rubric reward assigns 3× higher reward to proper spatial reasoning methodology.

Table 10. Base reasoning quality indicators (all tasks).

Indicator ϕ_i	Condition	w_i
Structured reasoning	≥ 2 step indicators (“Step 1”, “First”, “Then”)	+0.1
Conclusion statement	Contains conclusion phrase (“therefore”, “thus”)	+0.1
Reasoning consistency	Analysis logically supports final answer	+0.1
Reasoning inconsistency	Analysis contradicts final answer	-0.3

Table 11. Task-specific rubrics for `object_rel_direction`.

Indicator ϕ_i	Condition	w_i
<i>Positive Indicators</i>		
Coordinate extraction	Extracts ≥ 3 coordinate values	+0.10
Facing vector computation	Computes observer-to-target direction	+0.15
Local coordinate system	Constructs forward/right basis vectors	+0.25
Vector projection	Uses dot product for local components	+0.20
Quadrant determination	Maps component signs to quadrant	+0.10
<i>Negative Indicators</i>		
World-coordinate confusion	Uses $+x \rightarrow \text{right}$ without transform	-0.25
Missing transformation	Skips local frame construction	-0.20
Incorrect rotation	Wrong formula for right vector	-0.10
Incomplete 2D analysis	Checks only one axis	-0.10
Lucky guess	Correct answer without proper method	-0.30

Table 12. Task-specific rubrics for pairwise configuration.

Indicator ϕ_i	Condition	w_i
<i>Positive Indicators</i>		
Perspective-based reasoning	Uses object’s perspective, not viewer’s	+0.15
Orientation awareness	Considers yaw angle in analysis	+0.15
Coordinate analysis	Compares object coordinates correctly	+0.10
Directional consistency	Handles opposite pairs (left/right)	+0.10
<i>Negative Indicators</i>		
Viewer-centric error	Uses viewer perspective instead of object	-0.15
Orientation ignorance	Ignores yaw when determining directions	-0.15

B. Parameter Count Clarification and Scaling Analysis

B.1. Model Parameter Breakdown

Our full model introduces an additional spatial encoder ϕ beyond the base VLM. The complete parameter breakdown is as follows:

Table 13. Parameter breakdown of our full model.

Component	Parameters
SAM2 Encoder (Hiera-ViT-L)	214M
DA3 Encoder (ViT-G)	1.43B
Qwen3-VL-4B (LM backbone)	~4B
Total	~5.6B

A natural question arises: *given a fixed parameter budget, is it more effective to scale the spatial encoder or the language model?* We investigate this through the following experiments.

B.2. Parameter Allocation: Spatial Encoder vs. Language Model

Setup. We compare our model against Qwen3-VL-8B, which allocates an additional 4B parameters to the language model rather than the spatial encoder. This comparison isolates the effect of parameter allocation strategy. † denotes that we use the subsets for analysis (Object_rel_direction for VSI-Bench and Pairwise_configuration for Video-RoboSpatial).

Table 14. Parameter allocation comparison. Despite fewer total parameters (~5.6B vs. ~8B), allocating capacity to the spatial encoder outperforms scaling the language model.

Model	Total Param.	Spatial Enc.	LM	VSI-Bench (Avg 8)
Qwen3-VL-8B	8B	0	8B	55.1
Ours	5.6B	1.6B	4B	60.8 (+2.9%)

Finding 1

Allocating parameters to the spatial encoder yields greater improvements on spatial reasoning tasks than scaling the language model. Despite having fewer total parameters, our model outperforms Qwen3-VL-8B by 2.9% average accuracy on VSI-bench suggesting that spatial understanding is bottlenecked by encoder capacity rather than language modeling capacity.

C. Spatial Encoding Details

In this section, we provide additional implementation details about multi-frame fusion strategy (§C.1), 3D head design (§C.3) and training objectives (§C.4).

C.1. Multi-Frame 3D Detection Fusion

Our method predicts 3D bounding boxes in the camera coordinate system for each RGB frame. To obtain scene-level predictions, we transform per-frame detections into a unified world coordinate system and merge overlapping predictions across frames. This section details the transformation pipeline and spatial clustering strategy.

Given a sequence of T RGB frames with known camera poses $\{\mathbf{T}_1, \mathbf{T}_2, \dots, \mathbf{T}_T\}$, our Spatial Encoder predicts spatial codes for each frame in its respective camera coordinate system. For frame t , the output is $\mathbf{c}^t = \{\mathbf{c}_i^t\}_{i=1}^{n_t}$, where each spatial code is:

$$\mathbf{c}_i^t = (l_i^t, \mathbf{p}_i^t, \mathbf{s}_i^t, \mathbf{r}_i^t), \quad (14)$$

with semantic label l_i^t , position $\mathbf{p}_i^t \in \mathbb{R}^3$, size $\mathbf{s}_i^t \in \mathbb{R}^3$, and orientation (quaternion) $\mathbf{r}_i^t \in \mathbb{R}^4$.

The goal is to aggregate these per-frame predictions into a single set of scene-level spatial codes $\mathbf{c}^* = \{\mathbf{c}_i^*\}_{i=1}^{n^*}$ in world coordinates, where $n^* \ll \sum_{t=1}^T n_t$.

Spatial Clustering for Code Fusion Two spatial codes \mathbf{c}_i and \mathbf{c}_j (in world coordinates) are considered to represent the same object if they satisfy both:

- **Spatial Proximity.** The Euclidean distance between their positions is below a threshold:

$$\|\mathbf{p}_i - \mathbf{p}_j\| < \tau_{\text{dist}} \quad (15)$$

where $\tau_{\text{dist}} = 0.3$ meters. This criterion quickly filters out clearly distinct objects.

- **Geometric Overlap.** Among spatially proximate pairs, we require sufficient 3D overlap:

$$\text{IoU}_{3D}(\mathbf{c}_i, \mathbf{c}_j) > \tau_{\text{iou}}, \quad (16)$$

where $\tau_{\text{iou}} = 0.3$. This ensures that only geometrically consistent detections are merged.

3D IoU Computation For oriented 3D bounding boxes defined by position \mathbf{p} , size $\mathbf{s} = [w, h, l]^T$, and orientation \mathbf{r} , we compute the Intersection over Union as:

$$\text{IoU}_{3D} = \frac{V_{\text{inter}}}{V_1 + V_2 - V_{\text{inter}}}. \quad (17)$$

The intersection volume V_{inter} is computed by:

1. Projecting both boxes onto the ground plane (bird’s eye view) to compute the 2D intersection area A_{BEV} using convex hull intersection
2. Computing the vertical overlap height h_{overlap} between the two boxes along the y -axis
3. Computing intersection: $V_{\text{inter}} = A_{\text{BEV}} \times h_{\text{overlap}}$

Additionally, individual box volumes are computed from their sizes: $V = w \times h \times l$.

Cluster Aggregation For each cluster of N detections $\{\mathbf{c}_1, \dots, \mathbf{c}_N\}$ identified as representing the same object, we compute the representative spatial code by averaging their parameters at the scene-level:

$$\begin{aligned} \bar{\mathbf{p}} &= \frac{1}{N} \sum_{i=1}^N \mathbf{p}_i, \\ \bar{\mathbf{s}} &= \frac{1}{N} \sum_{i=1}^N \mathbf{s}_i, \\ \bar{\mathbf{r}} &= \text{QuaternionMean}(\{\mathbf{r}_1, \dots, \mathbf{r}_N\}), \end{aligned} \quad (18)$$

where orientations (quaternions) are averaged with proper handling of quaternion sign ambiguity. The semantic label \bar{l} is selected by majority voting among $\{l_1, \dots, l_N\}$.

C.2. Evaluation Protocol

For evaluation against ground truth annotations, we perform bipartite matching between predicted and ground truth spatial codes using the Hungarian algorithm. The matching is based on maximizing the total 3D IoU:

$$\text{maximize} \sum_{i,j} \text{IoU}_{3D}(\mathbf{c}_i^{\text{pred}}, \mathbf{c}_j^{\text{gt}}) \cdot m_{ij}, \quad (19)$$

where $m_{ij} \in \{0, 1\}$ indicates whether prediction i is matched to ground truth j .

A matched pair is considered a true positive if:

$$\text{IoU}_{3D}(\mathbf{c}_i^{\text{pred}}, \mathbf{c}_j^{\text{gt}}) \geq \tau_{\text{eval}}, \quad (20)$$

where $\tau_{\text{eval}} \in \{0.25, 0.50\}$ depending on the evaluation metric (F1@25 or F2@50).

C.3. 3D Head Design

Our 3D Head composes a series of transformer layers and MLPs predicting multiple spatial attributes through specialized prediction heads.

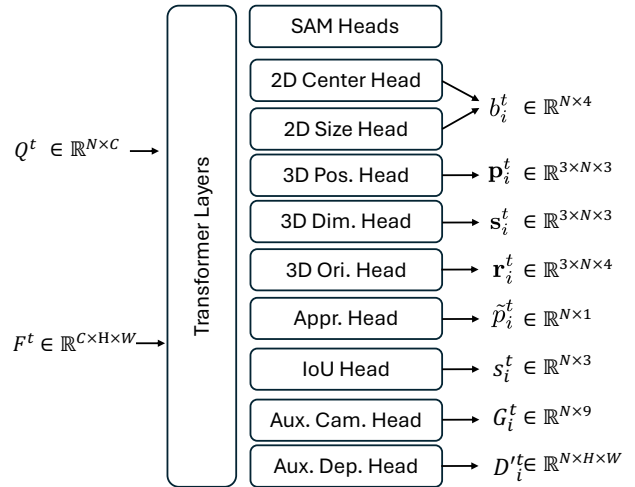


Figure 8. The details of 3D Head implementation.

We retain SAM’s original mask heads and use it for tracking, as implemented in (Ravi et al., 2024). The detection heads predict 3D bounding boxes: a 2D box head predicts normalized center coordinates and log-space width/height for 2D bounding box b_i^t ; per-mask 3D box heads output scaled (x_i^t, y_i^t) translation, log-space Z depth (z_i^t) and dimensions (sx_i^t, sy_i^t, sz_i^t) , and confidence c_i^t ; orientation is predicted through normalized quaternion representations. All spatial predictions $(x_i^t, y_i^t, z_i^t, sx_i^t, sy_i^t, sz_i^t)$ are scaled by a learned scale factor to handle metric ambiguity. Following SAM (Kirillov et al., 2023; Ravi et al., 2024), we implement three separate heads with an additional IoU head to output the confidence of each head. During inference, we choose the prediction with highest confidence.

We also include an auxiliary camera head and auxiliary depth head for geometry supervision, enforcing the feature to be aware of spatial information conditioned on $h_\phi^{\text{dep}}(F_i)$. This auxiliary camera prediction and depth map prediction are fused with the output of depth head by a factor of 0.1.

C.4. Training Objective Details

The detection loss $\mathcal{L}_{\text{Detection}}$ supervises frame-wise bounding box prediction. Following (Zhang et al., 2025; Brazil et al., 2023; Yang et al., 2025c), the 2D detection loss is a combination of GIoU loss and L1 loss between predicted 2D boxes and ground-truth 2D boxes, as:

$$\mathcal{L}_{2D \text{ det}} = \lambda_1 \cdot (1 - \text{GIoU}(\hat{b}_{2D}^t, b_{2D}^t)) + \lambda_2 \cdot \|\hat{b}_{2D}^t - b_{2D}^t\|. \quad (21)$$

For position $\mathbf{p}_i^t = (x_i^t, y_i^t, z_i^t)$, we project (x_i^t, y_i^t) in to pixel space by predicted intrinsics K , and use L1 loss to align it with ground-truth object center (\hat{x}_i, \hat{y}_i) in pixel space, while aligning predicted z_i^t with the real value \hat{z}_i by a Laplacian Aleatoric Uncertainty loss:

$$\begin{aligned} \mathcal{L}_{\text{pos}} = & \lambda_3 \cdot \|(\hat{x}_i^t, \hat{y}_i^t) - K \cdot (x_i^t, y_i^t)\| \\ & + \lambda_4 \cdot (\sqrt{2} \cdot e^{-u_z} \cdot \|\hat{z}_i - z_i^t\| + u_z). \end{aligned} \quad (22)$$

For object size prediction, L1 losses are applied to between predicted dimensions and ground-truth dimensions. For orientation, the prediction is represented as quaternions and L1 loss is applied after normalization. To ensure corner-wise alignment, a chamfer loss is implemented:

$$\mathcal{L}_{\text{chamfer}} = \frac{1}{|\mathcal{C}_i|} \sum_{\mathbf{c} \in \mathcal{C}_i} \min_{\hat{\mathbf{c}} \in \hat{\mathcal{C}}_i} \|\mathbf{c} - \hat{\mathbf{c}}\|_2 + \frac{1}{|\hat{\mathcal{C}}_i|} \sum_{\hat{\mathbf{c}} \in \hat{\mathcal{C}}_i} \min_{\mathbf{c} \in \mathcal{C}_i} \|\hat{\mathbf{c}} - \mathbf{c}\|_2, \quad (23)$$

where \mathcal{C}_i and $\hat{\mathcal{C}}_i$ denote the sets of predicted and ground-truth 3D bounding box corners for object i , respectively. To select the most confident head out of three predicted heads, we train an additional head to predict the 3D IoU score of each head:

$$\mathcal{L}_{3D \text{ IoU}} = \frac{1}{|\mathcal{V}|} \sum_{i \in \mathcal{V}} \sum_{k=1}^3 \left\| \hat{s}_i^k - \text{IoU}_{3D}(\mathcal{B}_{i,k}^t, \hat{\mathcal{B}}_i^t) \right\|_1, \quad (24)$$

where each \mathcal{B}_i^t is calculated from $(\mathbf{p}_i^t, \mathbf{s}_i^t, \mathbf{r}_i^t)$.

The geometry loss supervises depth prediction and camera pose prediction. Following (Wang et al., 2025a; Lin et al., 2025; Wang et al., 2024), we use scale-invariant depth loss with an aleatoric-uncertainty term and a gradient term for depth map prediction:

$$\begin{aligned} \mathcal{L}_{\text{depth}} = & \sqrt{\frac{1}{H \times W} \sum_i \left(e^{D_{\text{conf},i}^t} g_i^2 - D_{\text{conf},i}^t \right)} - \lambda \bar{g}^2 + \alpha \\ & + \|\tilde{D}^t - \hat{D}^t\|, \end{aligned} \quad (25)$$

where $g_i = \log(\tilde{D}_i^t + \alpha) - \log(\hat{D}_i^t + \alpha)$ denotes the log-depth difference at pixel i , $\bar{g} = \frac{1}{N} \sum_i g_i$ is its mean value, and $\tilde{D}^t = D^t / (\|D^t\|_2 + 1)$ represents the normalized predicted depth map. Here D_{conf}^t is the predicted confidence map that models aleatoric uncertainty, λ controls the scale-invariance penalty, and $\alpha = 10^{-7}$ ensures numerical stability.

The camera pose is encoded as $\mathbf{e}^t = [\mathbf{t}^t, \mathbf{q}^t, f^t]$, where $\mathbf{t}^t \in \mathbb{R}^3$ represents translation, $\mathbf{q}^t \in \mathbb{R}^4$ is the rotation quaternion, and f^t denotes the focal length. The camera loss consists of three components:

$$\mathcal{L}_{\text{camera}} = \lambda_T \cdot \|\hat{\mathbf{t}}^t - \mathbf{t}^t\|_1 + \lambda_R \cdot \|\hat{\mathbf{q}}^t - \mathbf{q}^t\|_1 + \lambda_f \cdot \|\hat{f}^t - f^t\|_1, \quad (26)$$

with λ_T , λ_R , and λ_f being the loss weights for translation, rotation, and focal length respectively. Here $\hat{\cdot}$ denotes ground truth values.

The tracking loss $\mathcal{L}_{\text{tracking}}$ supervises whether each object appears in the current frame, implemented as a sigmoid focal loss:

$$\mathcal{L}_{\text{tracking}} = -\frac{1}{N} \sum_{i=1}^N \alpha_t (1 - p_t)^\gamma \cdot \text{BCE}(\hat{p}_i^t, y_i), \quad (27)$$

where \hat{p}_i^t is the predicted appearance logit and $y_i \in \{0, 1\}$ indicates object presence.

C.5. Training-Free Implementation